





Hydrodynamically induced helical particle drift due to patterned surfaces

Danielle L. Chase^{a,1}, Christina Kurzthaler^{a,1} , and Howard A. Stone^{a,2} 

Edited by David Weitz, Harvard University, Cambridge, MA; received February 4, 2022; accepted May 15, 2022

Advances in microfabrication enable the tailoring of surfaces to achieve optimal sorting, mixing, and focusing of complex particulate suspensions in microfluidic devices. Corrugated surfaces have proved to be a powerful tool to manipulate particle motion for a variety of applications, yet the fundamental physical mechanism underlying the hydrodynamic coupling of the suspended particles and surface topography has remained elusive. Here, we study the hydrodynamic interactions between sedimenting spherical particles and nearby corrugated surfaces, whose corrugations are tilted with respect to gravity. Our experiments show three-dimensional, helical particle trajectories with an overall drift along the corrugations, which agree quantitatively with our analytical perturbation theory. The theoretical predictions reveal that the interaction of the disturbance flows, induced by the particle motion, with the corrugations generates locally a transverse anisotropy of the pressure field, which explains the helical dynamics and particle drift. We demonstrate that this dynamical behavior is generic for various surface shapes, including rectangular, sinusoidal, and triangular corrugations, and we identify surface characteristics that produce an optimal particle drift. Our findings reveal a universal feature inherent to particle transport near patterned surfaces and provide fundamental insights for future microfluidic applications that aim to enhance the focusing or sorting of particulate suspensions.

microfluidics | particle sedimentation | corrugated substrates | helical dynamics | near-surface drift

Interactions between particles and nearby boundaries make possible a variety of processes that depend, for example, on adsorption, reactions, or sensing (1–6). The optimal performance of these physical systems is crucially determined by the fluid-mediated coupling between the constituents in the flow and the confining surfaces. Thus, controlling and predicting hydrodynamic flows in microfluidic systems establish the foundation for various applications, such as mixing, sorting, and focusing of complex biological or synthetic samples (4–6). Unraveling the underlying physical mechanisms is expected to pave the way toward laboratory-on-a-chip devices for technological and biomedical applications, which aim, among others, toward the study of fundamental chemical and physical processes, the analysis of intracellular phenomena (7), and diagnostic tools for disease detection (8, 9).

Current microfluidic tools relevant for these applications rely on various physical principles, such as the filtration of specific constituents, or the use of external, e.g., magnetic, electric, or gravitational, fields for directed particle motion (4, 6, 10). Furthermore, the range of small-scale flows and geometries includes exploiting the emergence of hydrodynamic forces due to inertia (11–13); the presence of pillar arrays in a channel (14–16), i.e., a method referred to as “deterministic lateral displacement”; or the specific channel wall properties that can be, for example, elastic (17) or hydrophobically patterned (18). In addition, the use of corrugated or herringbone structures on channel walls has been demonstrated to allow for rapid mixing in pressure-driven laminar streams (19); the focusing of synthetic (20) and biological (21) constituents; and the separation of different, heterogeneous mixtures composed of, e.g., soft and stiff cells (22, 23), heavy and light colloids (20), or particles of different sizes (24, 25).

The latter topographically patterned systems exploit surface corrugations to generate transverse pressure gradients in pressure-driven microfluidic channel flow, which induce a helical circulation of the fluid streamlines. This phenomenon has received substantial attention (19, 20, 24, 25); however, the impact of the patterned surfaces on the motion of suspended particles has remained elusive. One common feature of these experiments is the observation of oscillatory, or “zig-zag,” particle trajectories drifting along the nearby corrugated walls (20, 21, 24, 25), yet the details of the underlying physics, the role of the patterned shape, and its consequences for, e.g., sorting and focusing, remain largely unaddressed.

Significance

Fluid–structure interactions are central to a large variety of microfluidic applications, ranging from the mixing of complex particulate suspensions to the sorting and focusing of biological samples. Here, we study the hydrodynamic coupling of particles with corrugated surfaces, which are widely used in different microfluidic settings. Combining experiments and theory, we reveal the full three-dimensional helical particle dynamics and identify the fundamental physical mechanisms leading to drift of the particle along the surface corrugations. We further identify an optimal drift and universal transport behavior as a function of the relevant length scales of our system. Our findings could enable optimization and enhanced sensitivity in existing microfluidic approaches for particle fractionation, focusing, and separation.

Author affiliations: ^aDepartment of Mechanical and Aerospace Engineering, Princeton University, Princeton, NJ 08544

Author contributions: D.L.C., C.K., and H.A.S. designed research, performed research, analyzed data, and wrote the paper.

The authors declare no competing interest.

This article is a PNAS Direct Submission.

Copyright © 2022 the Author(s). Published by PNAS. This article is distributed under [Creative Commons Attribution-NonCommercial-NoDerivatives License 4.0 \(CC BY-NC-ND\)](https://creativecommons.org/licenses/by-nc-nd/4.0/).

¹D.L.C. and C.K. contributed equally to this work.

²To whom correspondence may be addressed. Email: hastone@princeton.edu.

This article contains supporting information online at <https://www.pnas.org/lookup/suppl/doi:10.1073/pnas.2202082119/-/DCSupplemental>.

Published July 28, 2022.

To remove the effect of the helical fluid flow on particle transport in pressure-driven microfluidic channels with surface corrugations from the hydrodynamic coupling between the particle and the corrugated surface, the related scenario of particle sedimentation could provide physical insights. In this case, the primary driving force is gravity, rather than pressure gradients, although even here, the impact of surface corrugations has not been studied to date. Thus, the hydrodynamic coupling between suspended particles and nearby patterned surfaces poses a fundamental, open question in the field of transport at low Reynolds numbers, which is a feature of many physical systems.

Here, we use experiments and theory to study the sedimentation of spherical particles nearby corrugated surfaces, whose corrugations are tilted relative to the gravitational force. By monitoring the in-plane motion of the particles, our experiments reveal oscillatory, or zig-zag, particle dynamics with an overall drift along the surface corrugations, reminiscent of earlier experiments (20, 21, 24, 25). More importantly, we measure the full three-dimensional trajectories and demonstrate that surface corrugations, in fact, generate helical motion of spherical particles, which goes beyond the prevailing, mostly two-dimensional, picture of particle transport near surfaces and lays the foundation for elucidating the underlying physics. The particle trajectories and the physical mechanisms of this intricate behavior can be rationalized by a perturbation theory for the hydrodynamic flows. We further quantify, theoretically and experimentally, the particle drift as a function of surface shape and wavelength, which allows us to identify and unravel both an optimal and a universal transport behavior.

Results

Helical Particle Trajectories. We monitor spheres sedimenting in a viscous fluid near surfaces with corrugations that are tilted with respect to gravity (see Fig. 1 *A* and *B* and *Methods* for details of the experimental setup). First, we measure the in-plane motion of the particles (obtained from the front view [xy] of the experiment).

Our experiments show oscillatory, or zig-zag, particle trajectories near periodic, sinusoidal surfaces leading to an overall drift along the surface corrugations (Fig. 1 *C*). This dynamical behavior is reminiscent of earlier (unexplained) experimental observations of colloidal (20, 24, 25) and cellular transport (21) in pressure-driven flows nearby surface corrugations and, therefore, appears to be a phenomenon that is generic for a wide range of experimental systems involving patterned surfaces. Subsequently, we refer to motion along surface corrugations, if the particle moves in the direction of the negative y axis, and to motion across surface corrugations, if the particle moves in the direction of the positive y axis. Our findings demonstrate that a sphere drifts along the tilted surface corrugations, while sedimenting past a groove (dark background color in Fig. 1 *C*), and across the corrugations, while moving past a surface ridge (light background color in Fig. 1 *C*). The particle drifts significantly farther along the grooves than across the ridges, resulting in an overall drift perpendicular to the direction of gravity (forcing).

It is important to note that the particle is confined only by one surface in an otherwise unbounded domain. Most significantly, by tracking the particles in three dimensions, our experiments show that the particle trajectory exhibits helical motion (Fig. 1 *D*). It is well known that a sphere near a vertical planar wall sediments only parallel to the wall (and the gravitational field) (26, 27), and thus, the surface corrugations make this intricate observed behavior possible by generating motion perpendicular to the applied forcing. So far, helical trajectories have been observed only for sedimenting objects with, e.g., irregular (28, 29) and helical shapes (30). We demonstrate here that spheres can also follow a helical trajectory due to hydrodynamic coupling with the nearby surface structure.

To theoretically characterize the particle motion, we rely on the Stokes and continuity equations for the low Reynolds number hydrodynamic flows and a perturbation theory for a small surface roughness amplitude, which allows calculating the roughness-induced velocities of a spherical particle sedimenting near the surface corrugations (31) (see *Methods* for the theory and Fig. 1 *B*

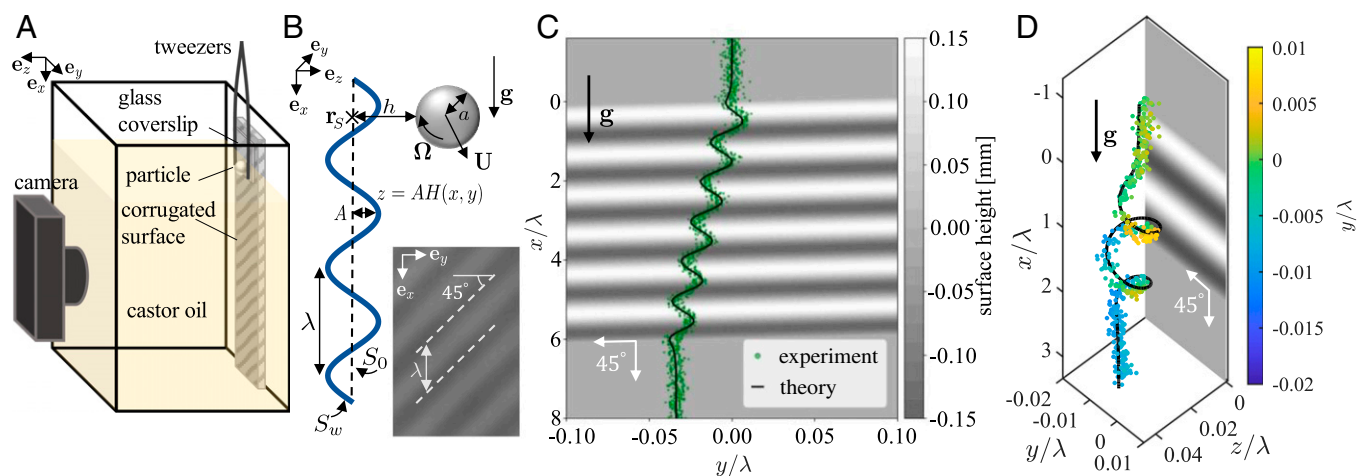


Fig. 1. Particle sedimentation near a corrugated surface. (A) Experimental setup. The particle is placed, using a tweezers, nearby the corrugated surface that is placed along one wall in a container of castor oil. Images are taken from the front (xy) and the side (xz , not shown) to track the particle motion. (B) Model setup. Shown is the side view of a spherical particle of radius a near a corrugated surface S_w , which is characterized by the shape function $H(x, y)$, wavelength λ , and amplitude A . The particle is at position $\mathbf{r}_S = (x_S, y_S)^T$ and a distance h from the reference surface S_0 . The sphere sediments due to gravity \mathbf{g} with translational and rotational velocities \mathbf{U} and $\mathbf{\Omega}$, respectively. Lower panel shows the front view of a 3D-printed surface with sinusoidal corrugations, which are tilted at an angle of 45° , with wavelength $\lambda = 6$ mm and amplitude $A = 0.15$ mm. (C) Two-dimensional experimental and theoretical trajectories of a spherical particle of radius $a = 1.5$ mm nearby periodic, sinusoidal corrugations with wavelength $\lambda = 6$ mm and amplitude $A = 0.15$ mm. The initial particle-surface distance is $h_0 \approx 0.15$ mm. The gray shaded areas indicate the height of the underlying surface. The surface corrugations are tilted at an angle of 45° . Note that the ranges of the x and y axes differ by two orders of magnitude ($x/\lambda \in [-1.6, 8]$ and $y/\lambda \in [-0.1, 0.1]$). (D) Three-dimensional experimental and theoretical helical trajectories of a spherical particle of radius $a = 1.6$ mm nearby a surface with two sinusoidal corrugations, tilted at an angle of 45° , of wavelength $\lambda = 6$ mm and amplitude $A = 0.15$ mm. The initial particle-surface distance is $h_0 \approx 0.2$ mm. The color scale indicates the y position of the particle.

for a model sketch). Our theoretical predictions of the particle trajectories quantitatively agree with our experimental measurements (Fig. 1 C and D). In particular, we find good agreement between our theory and experiments for both the in-plane motion and the full three-dimensional trajectories. Using this theoretical framework we can now understand the mechanism for the displacements.

Roughness-Induced Pressure and Flow Fields. While our findings, both experimental and with simulations, show that the sphere exhibits a helical trajectory and moves along the corrugations near grooves and across the corrugations near ridges, the underlying physics still pose an open, unexplained question, which we now address theoretically by deriving the roughness-induced hydrodynamic flow and pressure fields for the near-wall dynamics (*Methods* and *SI Appendix*).

Our findings suggest the following physical mechanism: As the particle sediments near the wall, it produces a disturbance flow and, consequently, interacts hydrodynamically with the nearby surface structure, $H(x, y)$. This interaction promotes the generation of a spatially varying pressure field (Fig. 2 A and B and *SI Appendix, Fig. S1 A and B*). In particular, the pressure field near a particle located above a surface groove, $x_S = 3\lambda/4$ (Fig. 2A), indicates a pressure decrease behind the particle and an increase of pressure in front of the particle, similar to what is expected for a sphere translating parallel to a planar wall (27). However, the presence of a nearby tilted surface ridge also generates a

transverse anisotropy in the pressure field at x_S (corresponding to $x/\lambda = 0$) along the y direction, which is larger for $y/\lambda > 0$ where the surface ridge in front of the particle is closer to the particle, and therefore we find that $\partial_y p^{(1)}(x_S, y_S; h) > 0$, where $p^{(1)}$ is the roughness-induced pressure. Consequently, the tilted surface ridge ‘pushes’ fluid (see Fig. 2C) and, consequently, the particle along the grooves (dark background color in Fig. 2C).

This picture changes for a particle located above a surface ridge, e.g., $x_S = 5\lambda/4$ (Fig. 2 B and D). In this case, the pressure is higher for $y/\lambda < 0$ [corresponding to $\partial_y p^{(1)}(x_S, y_S; h) < 0$], where, from the perspective of the sedimenting particle, the surface slope along the force direction is positive [$\partial_x H(x, y) > 0$], and lower for $y > 0$, where the slope is negative [$\partial_x H(x, y) < 0$], and hence the surface height decreases. The latter effectively opens up space for the fluid to flow (Fig. 2D), leading to particle motion across the ridge.

The generation of transverse anisotropy in the pressure field explains the oscillatory motion of the particle but does not yet explain the overall drift of the particle along the corrugations. To investigate this, we compute the transverse pressure gradient [$\partial_y p(x_S, y_S; h)$] along the particle trajectory C: $(x_S(t), y_S(t), h(t))$ of Fig. 1C. In particular, we find that the magnitude of the transverse pressure gradient produced by the particle as it moves in a groove is larger than that produced by the particle moving above a surface ridge. While sedimenting past a groove, the particle is on average closer to the ‘average’ surface, S_0 , than it is when sedimenting past a ridge (Fig. 3B), leading

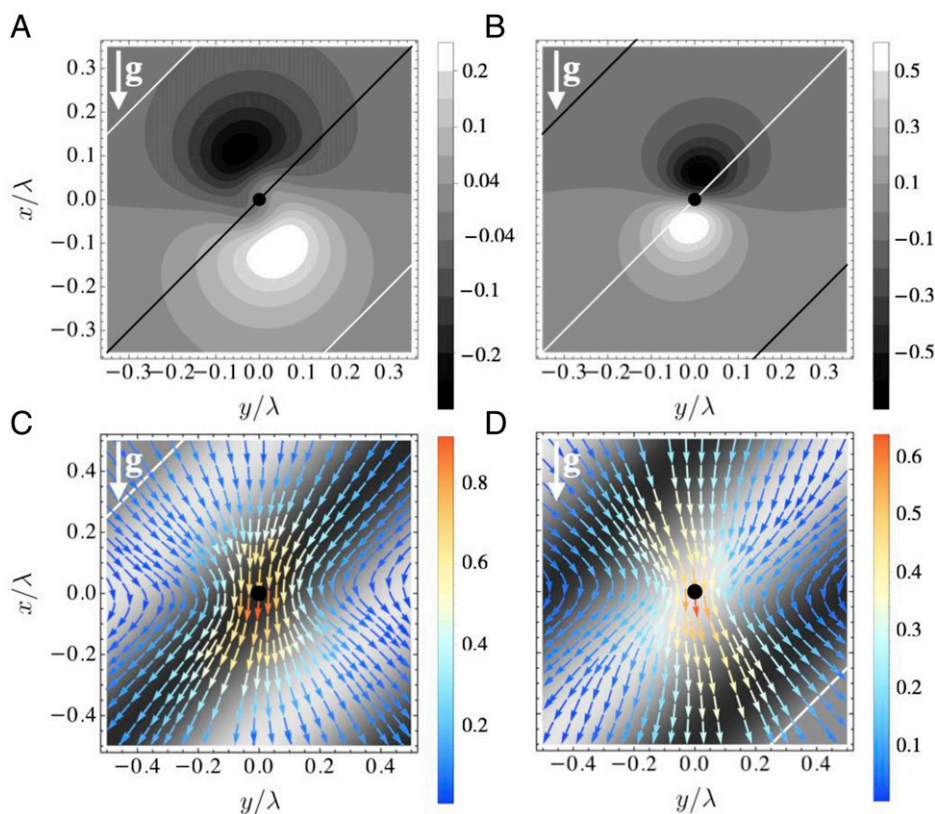


Fig. 2. Pressure and flow fields produced by a particle sedimenting near a surface with two sinusoidal corrugations. (A and B) Contour plots of the rescaled pressure $p/(\mu U_x^{(0)} \ell / h^2)$ with $\ell = \sqrt{2a\ell}$. The velocity of a sphere sedimenting near a planar wall is $U_x^{(0)} = 2\Delta\rho g a^2 / (9\mu \mathcal{R}_{\parallel}^{(0)})$, where g is the gravitational acceleration, $\Delta\rho = \rho_p - \rho_f$ is the density difference between the particle and the fluid, and $\mathcal{R}_{\parallel}^{(0)}$ is the dimensionless resistance to parallel motion due to the planar wall. The black and white lines indicate minima and maxima of the corrugated surface, respectively. (C and D) Streamlines of the flow fields $\mathbf{u}/U_x^{(0)}$ in the xy plane (at $z = 0.18$ mm) for the sphere located at $h = 0.2$ mm, $y_S = 0$, and two different positions: (A and C) $x_S = 3\lambda/4$ and (B and D) $x_S = 5\lambda/4$. Streamlines are colored according to the norm of the rescaled fluid velocity and gray shaded areas indicate the height of the underlying surface shape (color bar as in Fig. 1C). Here, x and y are measured from the particle center (x_S, y_S) , which is indicated as a black dot. We use geometric parameters $a = 1.5$ mm, $\lambda = 6$ mm, and $A = 0.15$ mm.

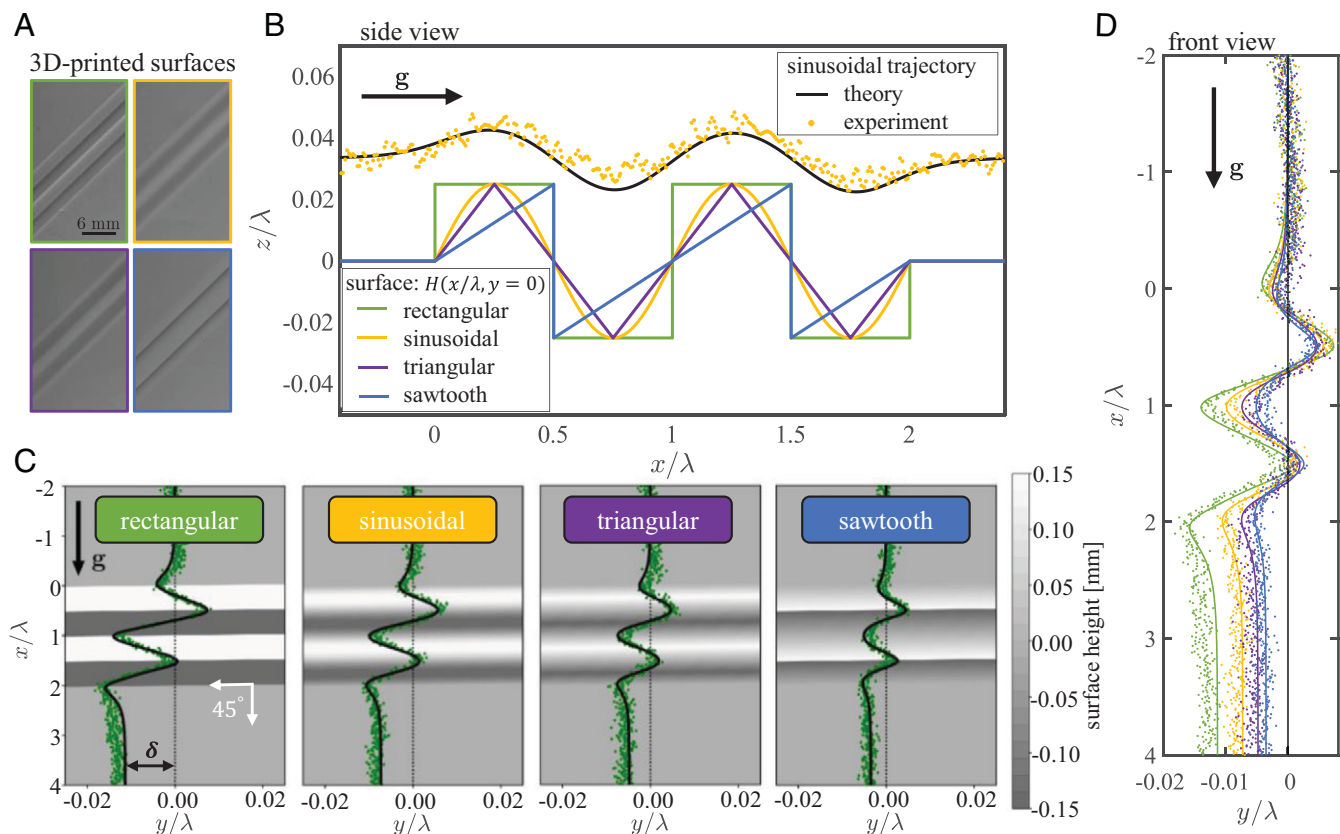


Fig. 3. Impact of corrugation shape on particle trajectories. (A) Images of 3D-printed surfaces with two corrugations of wavelength $\lambda = 6$ mm. From *Top Left*: rectangular, sinusoidal, triangular, and sawtooth shapes. (B) Side view (xz plane) of surface shapes and experimental (dots) and theoretical (black line) trajectories ($h(t), x_s(t)$), where $h(t)$ is the shortest distance between the particle surface and the reference surface S_0 , of a sedimenting particle (with $a = 1.6$ mm and $h_0 \simeq 0.2$ mm) along the sinusoidal surface. (C) Trajectories (xy plane) of particles (with $a = 1.6$ mm and $h_0 = 0.2$ mm) sedimenting near the surfaces in A. The green dots correspond to experiments and the black lines to the theory. δ is the lateral drift of the particle from its initial position. The surface corrugations are tilted at an angle of 45° . Note that the ranges of the x and y axes differ by two orders of magnitude ($x/\lambda \in [-2, 4]$ and $y/\lambda \in [-0.025, 0.025]$). (D) Comparison of the particle's lateral drift δ near different surface shapes (trajectories from C). Here, dots correspond to experiments and lines to the theoretical predictions.

to a symmetry breaking of the transverse pressure gradient with $\int_C \partial_y p^{(1)}(x_s, y_s; h) ds > 0$, where s is the arc length along the path C . Hence, the full three-dimensional information of the particle trajectory is required to elucidate the underlying physical mechanisms.

To study the dynamics of the helical trajectories in more detail, we first consider the effect of the shape of the surface corrugations and quantify particle trajectories near surfaces with two wavelengths of rectangular, sinusoidal, triangular, or sawtooth-shaped corrugations (Fig. 3A). In Fig. 3B and C, the trajectories are shown in the xz and xy planes, respectively (see *SI Appendix, Fig. S4* for the three-dimensional trajectories). Our perturbation theory quantitatively captures the three-dimensional experimental trajectories near these different shapes. We note that small deviations of the three-dimensional (3D)-printed surface structure (*SI Appendix, Fig. S.2*) or variation in the particle–surface distance (due to a tilt of the surface with respect to gravity or a nonplanar surface) are sources of experimental error when comparing the experimental results and theoretical predictions.

Irrespective of surface shape, the trajectories in the xy plane display oscillations, characterized by particle motion along the tilted corrugations near surface grooves and across them near ridges, and exhibit an overall drift δ along the corrugations (Fig. 3C). For all surface shapes, the turning point of the particle in the transverse direction occurs when the surface height vanishes $H(x, y) = 0$. The geometric details of the surface structure become manifest in the shape of the particle trajectory. We observe that the curvature of the turning point is related to the gradient of the surface height.

Very sharp turning points, corresponding to a large curvature of the particle trajectory, occur for the rectangular surface at all transitions between ridges and grooves and for the sawtooth surface where the surface height gradient is infinite, at $x/\lambda = 0.5$ and 1.5 . Alternatively, the turning point of the particle motion along the sawtooth surface at $x/\lambda = 1$, where the gradient is smaller, has a smaller curvature. The particle trajectories during turning for the sinusoidal and triangular surfaces show an intermediate curvature.

Our results further demonstrate that the overall drift δ depends on the shape of the surface grooves (Fig. 3D). Particles experience the largest drift sedimenting near the rectangular surface and experience the smallest drift sedimenting near the sawtooth surface. This result may be rationalized by the magnitude of the gradient of the height of the surface at the reversal point, as larger surface height gradients generate larger pressure gradients that push the particle along the grooves.

Trajectories as a Function of Surface Geometry. In addition to the shape of the surface corrugations, our system is characterized by three dimensionless geometric parameters:

$$\frac{\lambda}{a}, \quad \frac{A}{\lambda}, \quad \frac{h_0}{a} \left(\text{or } \frac{\langle h \rangle}{a} \right), \quad [1]$$

where h_0 denotes the initial particle–surface distance and $\langle h \rangle$ is the particle–surface distance averaged over the particle trajectory. Therefore, we investigate the drift of particles along corrugated sinusoidal surfaces by keeping the parameter $A/\lambda = 0.018$ fixed

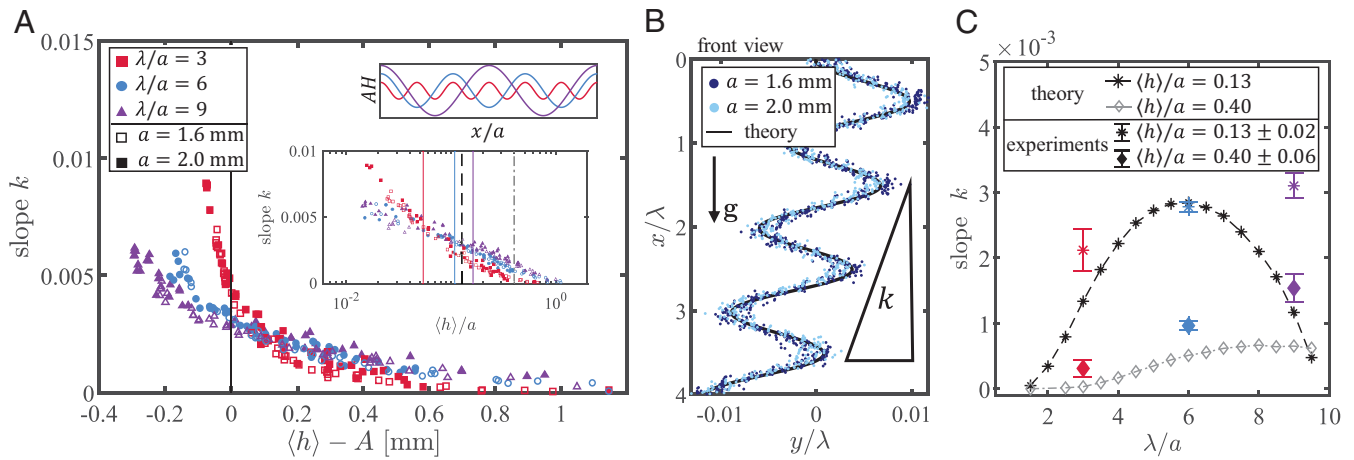


Fig. 4. Particle trajectories and drift as a function of surface geometry. (A) Slope of particle trajectories k as a function of $\langle h \rangle - A$ for $\lambda/a = 3, 6,$ and 9 (indicated by red squares, blue circles, and purple triangles, respectively). Open and solid symbols correspond to particle radii of 1.6 and 2.0 mm, respectively. Surfaces have sinusoidal corrugations oriented at 45° spanning the entire surface with $A/\lambda = 0.018$. *Upper Inset* shows the surface corrugations along x/a with height AH for $\lambda/a = 3, 6,$ and 9 . *Lower Inset* shows the slope k as a function of $\langle h \rangle/a$ for the same data. The solid colored lines indicate where the average particle–surface distance is the same as the surface amplitude, $\langle h \rangle/a = A/a$, for each value of λ/a . The black dashed line indicates $\langle h \rangle/a = 0.13$ and the gray dotted-dashed line indicates $\langle h \rangle/a = 0.4$. (B) Comparison of particle trajectories from data in A for $\lambda/a = 6$ and $\langle h \rangle/a = 0.13$. Experimental data are dark blue and light blue dots for $a = 1.6$ mm and $a = 2.0$ mm, respectively. The theoretical particle trajectory is shown by the solid black line. The slope of the trajectory is k . (C) Comparison of slopes k of experimental data from A at $\langle h \rangle/a = 0.13 \pm 0.02$ and $\langle h \rangle/a = 0.4 \pm 0.06$ with theoretical predictions of the slopes at $\langle h \rangle/a = 0.13$ and 0.4 . Asterisks and diamonds correspond to the data for $\langle h \rangle/a = 0.13$ and 0.4 , respectively. Error bars on experimental data indicate the SD of the measured slopes.

so that the surface height gradients are the same for surfaces with varying wavelength (Fig. 4A, *Upper Inset*). We conduct experiments with particles of radii $a = 1.6$ mm and $a = 2.0$ mm and surface wavelength-to-particle radius ratios $\lambda/a = 3, 6,$ and 9 . We now use periodic, sinusoidal surfaces with corrugations spanning the entire surface, allowing us to robustly extract the slope k of the trajectory.

Most significantly, we discover that the particle motion becomes universal for a fixed A/λ and given λ/a . This becomes manifest in the slope of the particle trajectories (Fig. 4A), where measurements of particles of two sizes (open and solid symbols) overlap for a given λ/a . In particular, we find good agreement between the trajectories for both particle sizes with the theoretical prediction (Fig. 4B and *SI Appendix, Fig. S5*), which demonstrates that the trajectories are fully determined by the three dimensionless parameters A/λ , λ/a , and $\langle h \rangle/a$.

Furthermore, we identify two regimes that dictate the overall particle drift. When the average particle–surface distance is inside of the surface corrugations, corresponding to $\langle h \rangle - A < 0$ (to the left of the solid black line in Fig. 4A), the shortest-wavelength surface ($\lambda/a = 3$) creates the largest drift. At $\langle h \rangle - A \simeq 0.1$ mm, when the particles move mostly outside of the surface corrugations, we observe a reversal of this trend. When the average particle–surface distance is outside of the surface corrugations (to the right of the purple line, $A/a = 0.16$, in Fig. 4A, *Lower Inset*), the longest-wavelength surface causes the largest drift.

To rationalize the change of the slope k as a function of λ/a , we compare the experimental observations to the theoretical prediction for $\langle h \rangle/a = 0.4$ and 0.13 (indicated by the gray dotted-dashed and black dashed lines in Fig. 4A, *Lower Inset*, respectively). Both theory and experiments for $\langle h \rangle/a = 0.4$ show a monotonic increase of the slope with increasing λ/a . For $\langle h \rangle/a = 0.13$, the theory predicts a nonmonotonic behavior of the slope as a function of λ/a and deviates from experiments at large λ/a or large A . In this regime, the theory breaks down as the average particle–surface distance becomes smaller than the surface amplitude, $\langle h \rangle - A < 0$, meaning that the particle enters the surface corrugations (see *Methods* for a derivation of the perturbation theory and its validity).

Optimal Particle Drift. Having established a quantitative understanding of the relevant nondimensional parameters of our system (Eq. 1), we now measure the overall particle drift for different wavelengths λ , by keeping the surface amplitude, $A = 0.15$ mm, and the particle radius, $a = 1$ mm, fixed (Fig. 5A). As before, we first consider surfaces with corrugations spanning the entire surface and vary the particle–surface distance $\langle h \rangle$. We find that particles nearest to the surface have a maximal slope k of their trajectories, which decreases as they move farther from the wall. In addition, we observe, reminiscent of our earlier findings (Fig. 4A), that the current system exhibits two distinct regimes: 1) For $\langle h \rangle/a \lesssim 0.2$, the particle begins to enter the surface corrugations ($A/a = 0.15$) and, therefore, experiences the largest drift for the smallest-wavelength surface, which has the steepest surface height

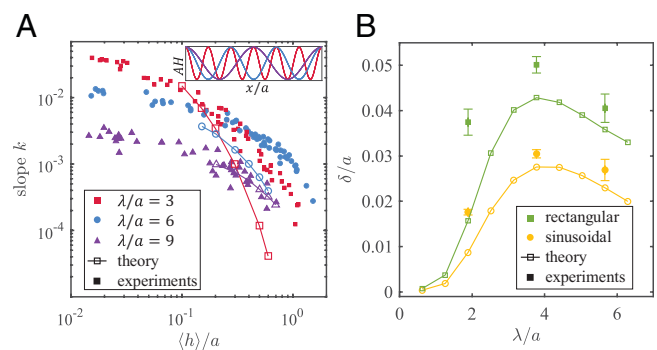


Fig. 5. Optimal particle drift. (A) Slope k of particle trajectories as a function of the average particle–surface distance $\langle h \rangle$. Open symbols connected by solid lines correspond to theoretical predictions and solid symbols are experimental measurements. Surfaces have sinusoidal corrugations, which are oriented at 45° , spanning the entire surface with amplitude $A = 0.15$ mm and varying wavelength λ . *Inset* shows the surface corrugations along x/a with height AH . (B) Particle drift δ induced by surface corrugations of different shapes as a function of the wavelength λ . Surfaces have two corrugations that are oriented at 45° (Fig. 3). Open symbols connected by solid lines correspond to theoretical predictions and solid symbols are experimental measurements for a particle at an initial particle–surface distance of $h_0 \simeq 0.2$ mm. Particles have a radius of $a = 1.6$ mm. Error bars on experimental data represent the SD of the measured drift for three different trajectories at each wavelength.

gradient (Fig. 5 *A*, *Inset*). 2) Most importantly, farther from the surface, $\langle h \rangle/a \gtrsim 0.2$, the intermediate-wavelength surface $\lambda/a = 6$ (Fig. 5*A*, blue circles) causes the largest drift. Both the theoretical predictions (open symbols) and the experimental measurements exhibit this cross-over to a nonmonotonic transport behavior.

To investigate the nonmonotonic particle drift in more detail, we consider surfaces with two corrugations of different shapes (rectangular and sinusoidal; Fig. 3 *A* and *B*), a particle of radius $a = 1.6$ mm, and a fixed initial distance $h_0 \simeq 0.2$ mm. Our findings show that the drift δ becomes maximal at $\lambda/a \sim 3$ to 4, depending on the surface shape (Fig. 5*B*). In particular, for small and large wavelengths λ the corrugated surface approaches the shape of a planar wall and, therefore, the drift becomes small. Both experiments and theory reveal that the overall drift for a rectangular surface shape is larger than that for a sinusoidal shape, irrespective of the surface wavelength λ/a and particle–surface separation distance h_0/a (not shown). These results demonstrate that the corrugation geometry can be tuned to optimize the transport behavior of the relevant constituents.

Conclusions

By combining sedimentation experiments with a perturbation theory, we have quantified the three-dimensional, helical particle trajectories and resulting drift of particles sedimenting nearby tilted surface corrugations of different shapes. We have demonstrated that the overall drift persists for various surface shapes and can be optimized as a function of shape and wavelength. Our theoretical findings further demonstrate that the helical near-surface dynamics are induced by anisotropic pressure fields, which result from the coupling of the hydrodynamic flows produced by the sedimenting particles with the surface corrugations. The projection of the three-dimensional helical particle motion to the two-dimensional oscillatory near-surface motion, as quantified here, has been observed in various other experiments, ranging from colloidal (20, 24, 25) to biological (21) samples. Therefore, we anticipate that it is a universal feature inherent to transport processes near patterned surfaces, which we have rationalized here using a hydrodynamic theory.

In this work, we identified helical transport behavior of spherical particles sedimenting close to surface corrugations. This behavior becomes perturbed by various aspects of the specific setup. In particular, as the sedimentation velocity of a sphere near a planar wall approaches that in an unbounded fluid (U_b) at large particle–surface distance, $h/a \gg 1$, as $U_x^{(0)}/U_b \simeq 1 - 9a/(16h)$ (32), we anticipate that the helical behavior becomes negligibly small at $(h - A)/a \gg 1$. Our study showed that at $(h - A)/a \simeq 1$ the slope of the trajectories is $\mathcal{O}(10^{-4})$.

While our experiments relied on the use of millimeter-sized particles, the predictions also apply for low-Reynolds-number flows at the micro- and nanoscales. At smaller scales, Brownian effects may become relevant, and we expect to observe a signature of helical transport behavior only as long as the time it takes for a particle with diffusivity D to diffuse one wavelength, λ^2/D , is much longer than the time it takes to cross one wavelength due to couplings with the surface roughness, $\lambda/(\epsilon U_x^{(0)})$, leading to $\epsilon \gg D/(\lambda U_x^{(0)}) \sim k_B T/(\lambda F_g)$, where $\epsilon = A/a$. Here, k_B is the Boltzmann constant, T is temperature, and F_g is the force acting on the sphere due to gravity. Equivalently, we find a criterion for the particle size such that Brownian effects are negligible: $a \gtrsim \sqrt{3k_B T/(4\pi\lambda A g \Delta\rho)}$, where g is the gravitational acceleration and $\Delta\rho$ denotes the density difference between the

particle and the fluid. For our system, we find that Brownian motion is negligible for a larger than ~ 1 nm. It could, however, become important for less dense colloids sedimenting at a lower velocity.

Moreover, we note that the helical behavior is expected to vanish if the roughness amplitude of the surface material β , which appears as a randomly structured surface on top of the corrugations (31), is of the same order as the surface amplitude, $\beta \simeq A$. In this case, hydrodynamic coupling with the surface heterogeneities entails a change of the particle velocities and randomizes the particle motion.

Future research should address the impact of pressure-driven flows, herringbone surface structures (19–21), particle shape (33, 34), and elasticity (22, 23) on the helical transport behavior and near-surface drift, which could pave the way toward novel technologies for the sorting and focusing of particles or biological cells. The latter could allow for a noninvasive visualization of cells and the study of intracellular biological processes. Furthermore, our study has revealed that details of the surface manifest themselves in the particle trajectories, which may allow for a characterization of surface properties, reminiscent of “passive microrheology.” We further anticipate that the addition of local microstructures to existing sensing systems could help to steer particles toward sensors and thereby enhance their signal for technological applications.

Methods

Experimental Methods. In our experiments, 3D-printed corrugated surfaces (2.5×10.5 cm) are placed vertically in a container ($8.5 \times 8.5 \times 10.5$ cm) of castor oil (density $\rho = 950$ kg \cdot m $^{-3}$ and viscosity $\mu = 0.85$ Pa \cdot s) (Fig. 1*A*). We use stereolithography (Formlabs Form 2) to fabricate two types of corrugated surfaces (see *SI Appendix* for details of the 3D-printing process). One type of surface has flat sections before the corrugations begin and after they stop (with corrugations having various shapes and wavelengths). These surfaces are used for Figs. 1 *C* and *D*, 2, 3, and 5*B*. In general, these surfaces are advantageous for measuring the detailed particle trajectories and the particle displacement δ , as the particle has a defined initial and final z position. The second type of surface (Figs. 4 and 5*A*) does not have the flat sections, and instead the corrugations span the entire length of the surface. These surfaces enable a more robust measurement of the slope k of the particle’s trajectory. We are restricted to either having the flat sections before and after few corrugations or having no flat section but many corrugations because the total sedimentation length that can be imaged by the camera is limited. All corrugations are oriented at 45° relative to gravity, \mathbf{g} (Fig. 1*B*). We examine the effect of changing the corrugation angle in *SI Appendix*, Fig. *S6*.

Using a tweezers, a particle (Delrin acetal resin [McMaster-Carr]) is placed nearby the corrugated surface just below the oil–air interface and then released. Since our system is at a low Reynolds number, the effect of the tweezers on the flow is important only at small time and length scales. To minimize the effect of the initial release, we allow the particle to sediment ~ 10 times its radius before recording its trajectory. In some experiments, to control the initial distance of the particle relative to the surface, we adhere coverslips of varying thicknesses near the top of the corrugated surface and place the particle in contact with the coverslip.

We image the trajectory of the particle at 30 frames per second from the front and the side to track its position in the xy and xz planes, respectively. Images are processed using MATLAB (MathWorks) to find the position of the particle in each frame.

We use two methods to measure the particle–surface distance h_0 or $\langle h \rangle$. For the printed surfaces with flat sections before the surface corrugations, we measure the distance between the particle and the flat wall, h_0 , from the side view. For surfaces with corrugations spanning the entire surface, we find the average particle–surface distance $\langle h \rangle$ over the particle’s entire trajectory by measuring the ratio of the particle’s settling speed U_w , relative to the settling speed in bulk U_b ,

and infer the ratio $\langle h \rangle / a$ from the theoretical prediction of the velocity of a sphere near a planar wall (see *SI Appendix* and *SI Appendix, Fig. S3* for the validation of this method).

Theory: Roughness-Induced Velocities, Pressure, and Flow Fields. To theoretically characterize the particle motion, we consider a sphere of radius a sedimenting with translational velocity \mathbf{U} and rotating at angular velocity $\boldsymbol{\Omega}$ nearby a corrugated surface, S_w . The particle is located at a distance h and position $\mathbf{r}_S = (x_S, y_S)^T$ with respect to a planar reference surface S_0 (Fig. 1B). The corrugated surface is described by $z = AH(x, y)$ with shape function $H(x, y)$ and amplitude A . The flow and pressure fields, $\mathbf{u}(x, y, z)$ and $p(x, y, z)$, obey the Stokes and continuity equations,

$$\mu \nabla^2 \mathbf{u} = \nabla p \quad \text{and} \quad \nabla \cdot \mathbf{u} = 0. \quad [2]$$

In the comoving frame of reference attached to the particle, the no-slip boundary conditions are $\mathbf{u} = -\mathbf{U}$ on the corrugated surface S_w and S_∞ , which denotes the bounding surface at infinity, and $\mathbf{u} = \boldsymbol{\Omega} \wedge \mathbf{r}$ on the surface of the sphere S_p . Subsequently, we consider a small surface amplitude with $A = \epsilon a \ll h$, which allows expanding the flow and pressure fields in the small parameter ϵ , i.e., $\mathbf{u} = \mathbf{u}^{(0)} + \epsilon \mathbf{u}^{(1)} + \mathcal{O}(\epsilon^2)$ and $p = p^{(0)} + \epsilon p^{(1)} + \mathcal{O}(\epsilon^2)$, and similarly the translational and rotational velocities, $\mathbf{U} = \mathbf{U}^{(0)} + \epsilon \mathbf{U}^{(1)} + \mathcal{O}(\epsilon^2)$ and $\boldsymbol{\Omega} = \boldsymbol{\Omega}^{(0)} + \epsilon \boldsymbol{\Omega}^{(1)} + \mathcal{O}(\epsilon^2)$. Furthermore, we can simplify the boundary condition via a domain perturbation approach (31, 35) and arrive at $\mathbf{u}^{(0)} = -\mathbf{U}^{(0)}$ on S_0 and

$$\mathbf{u}^{(1)} = -\mathbf{U}^{(1)} - aH(x, y) \frac{\partial \mathbf{u}^{(0)}}{\partial z} \Big|_{z=0} \equiv \mathbf{u}_{S_0}^{(1)} \quad \text{on } S_0, \quad [3]$$

where we have introduced the effective slip velocity at the planar wall $\mathbf{u}_{S_0}^{(1)}$. Here, $\mathbf{u}^{(0)}$ denotes the flow field produced by the sedimentation of a sphere near a planar wall, which can be obtained analytically for arbitrary h/a using a bispherical coordinate representation (26, 36–38). Following our previous work (31), we exploit the Lorentz reciprocal theorem (39, 40), which relates two problems with the same geometry but different boundary conditions, to compute the roughness-induced velocities, $\mathbf{U}^{(1)}$ and $\boldsymbol{\Omega}^{(1)}$. Therefore, we introduce as an auxiliary problem a sphere translating and rotating near a planar wall with associated velocity and pressure fields, $\hat{\mathbf{u}}$ and \hat{p} , respectively. The reciprocal partially theorem (39, 40) then relates the auxiliary problem, with $\hat{\mathbf{u}}$ and stress field $\hat{\boldsymbol{\sigma}} = -\hat{p}\mathbf{I} + (\nabla \hat{\mathbf{u}} + (\nabla \hat{\mathbf{u}})^T)/2$, to our first-order problem, with $\mathbf{u}^{(1)}$ and $\boldsymbol{\sigma}^{(1)}$, via

$$\int_S \mathbf{n} \cdot \boldsymbol{\sigma}^{(1)} \cdot \hat{\mathbf{u}} \, dS = \int_S \mathbf{n} \cdot \hat{\boldsymbol{\sigma}} \cdot \mathbf{u}^{(1)} \, dS. \quad [4]$$

Here, we abbreviated the sum of all surfaces by $S = S_0 \cup S_p \cup S_\infty$ and \mathbf{n} is the outward-pointing normal vector to the surface.

1. D. J. Beebe, G. A. Mensing, G. M. Walker, Physics and applications of microfluidics in biology. *Annu. Rev. Biomed. Eng.* **4**, 261–286 (2002).
2. J. El-Ali, P. K. Sorger, K. F. Jensen, Cells on chips. *Nature* **442**, 403–411 (2006).
3. E. K. Sackmann, A. L. Fulton, D. J. Beebe, The present and future role of microfluidics in biomedical research. *Nature* **507**, 181–189 (2014).
4. H. A. Stone, A. D. Stroock, A. Ajdari, Engineering flows in small devices: Microfluidics toward a lab-on-a-chip. *Annu. Rev. Fluid Mech.* **36**, 381–411 (2004).
5. G. M. Whitesides, The origins and the future of microfluidics. *Nature* **442**, 368–373 (2006).
6. C. W. Shields 4th, C. D. Reyes, G. P. López, Microfluidic cell sorting: A review of the advances in the separation of cells from debulking to rare cell isolation. *Lab Chip* **15**, 1230–1249 (2015).
7. S. Hoscic, S. K. Murthy, A. N. Koppes, Microfluidic sample preparation for single cell analysis. *Anal. Chem.* **88**, 354–380 (2016).
8. S. L. Stott *et al.*, Isolation of circulating tumor cells using a microvortex-generating herringbone-chip. *Proc. Natl. Acad. Sci. U.S.A.* **107**, 18392–18397 (2010).
9. A. Farahinia, W. Zhang, I. Badae, Novel microfluidic approaches to circulating tumor cell separation and sorting of blood cells: A review. *J. Sci.-Adv. Mater. Dev.* **6**, 303–320 (2021).

Simplifying Eq. 4 (see ref 31 for details), we obtain the velocities of a sphere near a corrugated wall via $(\mathbf{U}, \boldsymbol{\Omega})^T = \mathbf{M} \cdot (\mathbf{F}, \mathbf{L})^T$, where \mathbf{F} and \mathbf{L} denote the applied force and torque, and the mobility obeys

$$\mathbf{M} = \mathbf{M}^{(0)} - \epsilon \int_{S_0} aH(x, y) \mathbf{K} dS + \mathcal{O}(\epsilon^2). \quad [5]$$

Here, the second term on the right-hand side corresponds to the roughness-induced mobility and the coupling tensor \mathbf{K} depends on the zeroth-order problem only (31). To calculate trajectories of sedimenting particles, we set $\mathbf{F} = \mathbf{F}_g$, which denotes the force on the particle due to gravity, and $\mathbf{L} = \mathbf{0}$. We compute the mobility (Eq. 5) by relying on a bispherical coordinate representation of $\mathbf{u}^{(0)}$, $p^{(0)}$ and $\hat{\mathbf{u}}$, \hat{p} (26, 36–38) and evaluate the integral numerically. Details can be found in the supplemental material of ref. 31, where a validation of our theory with a boundary integral method is presented.

We then numerically evaluate the equation of motion, $d\mathbf{r}/dt = \mathbf{U}^{(0)} + \epsilon \mathbf{U}^{(1)}$, where t denotes time and the instantaneous particle position is $\mathbf{r}(t) = (x_S(t), y_S(t), h(t))^T$.

In addition, we derive the roughness-induced pressure and flow fields. Therefore, we consider the lubrication regime, i.e., $h/a \ll 1$, which allows simplifying the Stokes and continuity equations (Eq. 2). To leading order in h/a , the zeroth-order problem $\mathbf{u}^{(0)}$ is well known (27, 41, 42). To calculate $\mathbf{u}^{(1)}$ we first derive the “generalized” Reynolds equation for the roughness-induced pressure $p^{(1)}$ (see *SI Appendix* for a detailed derivation), again working in the reference frame of the particle:

$$0 = \mathbf{U}^{(1)} \cdot \mathbf{e}_z + \frac{h_p^3}{6\mu} \nabla_{\parallel}^2 p^{(1)} + h_p \nabla_{\parallel} \cdot \mathbf{u}_{S_0}^{(1)} - \frac{h_p^2}{2} \nabla_{\parallel} \cdot \left(\frac{h_p}{2\mu} \nabla_{\parallel} p^{(1)} + \frac{\mathbf{u}_{S_0}^{(1)} + a\boldsymbol{\Omega}^{(1)} \wedge \mathbf{e}_z}{h_p} \right), \quad [6]$$

where the surface of the sphere is approximated by a parabola $h_p(x, y) = h + (x^2 + y^2)/(2a)$ and we have abbreviated the in-plane gradient by $\nabla_{\parallel} = (\partial/\partial x, \partial/\partial y, 0)^T$. Eq. 6 further depends on the effective slip at the planar wall, $\mathbf{u}_{S_0}^{(1)}$, which is obtained from the zeroth-order flow field within the lubrication approximation via Eq. 3. Using the roughness-induced velocities $\mathbf{U}^{(1)}$ and $\boldsymbol{\Omega}^{(1)}$ as input, we solve Eq. 6 for $p^{(1)}(x, y)$ numerically with a finite-element method [in Mathematica (43)] and compute the flow field $\mathbf{u}^{(1)}(x, y, z)$. Details of the numerical evaluation are provided in *SI Appendix*.

Data Availability. Source data and computer code are available on GitHub at https://github.com/ckurzthaler/materials_sedimentation_patterned_surface (44).

ACKNOWLEDGMENTS. We thank Amir A. Pahlavan for helpful discussions at the initial stage of this project. D.L.C. acknowledges support from the NSF Graduate Research Fellowship Program and the High Meadows Environmental Institute at Princeton University through the Walbridge Fund. C.K. acknowledges support from the Austrian Science Fund (Fonds zur Förderung der wissenschaftlichen Forschung) via the Erwin Schrödinger fellowship (Grant J4321-N27). This work was supported by NSF Grant MCB-1853602 (to H.A.S.).

10. J. C. Giddings, Field-flow fractionation: Analysis of macromolecular, colloidal, and particulate materials. *Science* **260**, 1456–1465 (1993).
11. G. Segré, A. Silberberg, Radial particle displacements in Poiseuille flow of suspensions. *Nature* **189**, 209–210 (1961).
12. D. Di Carlo, D. Irimia, R. G. Tompkins, M. Toner, Continuous inertial focusing, ordering, and separation of particles in microchannels. *Proc. Natl. Acad. Sci. U.S.A.* **104**, 18892–18897 (2007).
13. K. J. Humphry, P. M. Kulkarni, D. A. Weitz, J. F. Morris, H. A. Stone, Axial and lateral particle ordering in finite Reynolds number channel flows. *Phys. Fluids* **22**, 081703 (2010).
14. L. R. Huang, E. C. Cox, R. H. Austin, J. C. Sturm, Continuous particle separation through deterministic lateral displacement. *Science* **304**, 987–990 (2004).
15. J. A. Davis *et al.*, Deterministic hydrodynamics: Taking blood apart. *Proc. Natl. Acad. Sci. U.S.A.* **103**, 14779–14784 (2006).
16. J. McGrath, M. Jimenez, H. Bridle, Deterministic lateral displacement for particle separation: A review. *Lab Chip* **14**, 4139–4158 (2014).
17. B. Rallabandi, N. Oppenheimer, M. Y. B. Zion, H. A. Stone, Membrane-induced hydroelastic migration of a particle surfing its own wave. *Nat. Phys.* **14**, 1211 (2018).

18. E. S. Asmolov, A. L. Dubov, T. V. Nizkaya, A. J. C. Kuehne, O. I. Vinogradova, Principles of transverse flow fractionation of microparticles in superhydrophobic channels. *Lab Chip* **15**, 2835–2841 (2015).
19. A. D. Stroock *et al.*, Chaotic mixer for microchannels. *Science* **295**, 647–651 (2002).
20. C. H. Hsu, D. Di Carlo, C. Chen, D. Irimia, M. Toner, Microvortex for focusing, guiding and sorting of particles. *Lab Chip* **8**, 2128–2134 (2008).
21. M. A. Qasimeh *et al.*, Isolation of circulating plasma cells in multiple myeloma using CD138 antibody-based capture in a microfluidic device. *Sci. Rep.* **7**, 45681 (2017).
22. B. Tasadduq, W. Lam, A. Alexeev, A. F. Sarioglu, T. Sulchek, Enhancing size based size separation through vertical focus microfluidics using secondary flow in a ridged microchannel. *Sci. Rep.* **7**, 17375 (2017).
23. G. Wang *et al.*, Microfluidic cellular enrichment and separation through differences in viscoelastic deformation. *Lab Chip* **15**, 532–540 (2015).
24. S. Choi, J. K. Park, Continuous hydrophoretic separation and sizing of microparticles using slanted obstacles in a microchannel. *Lab Chip* **7**, 890–897 (2007).
25. S. Choi, T. Ku, S. Song, C. Choi, J. K. Park, Hydrophoretic high-throughput selection of platelets in physiological shear-stress range. *Lab Chip* **11**, 413–418 (2011).
26. M. E. O'Neill, A slow motion of viscous liquid caused by a slowly moving solid sphere. *Mathematika* **11**, 67–74 (1964).
27. A. J. Goldman, R. G. Cox, H. Brenner, Slow viscous motion of a sphere parallel to a plane wall—I motion through a quiescent fluid. *Chem. Eng. Sci.* **22**, 637–651 (1967).
28. M. Doi, M. Makino, Sedimentation of particles of general shape. *Phys. Fluids* **17**, 043601 (2005).
29. N. W. Krapf, T. A. Witten, N. C. Keim, Chiral sedimentation of extended objects in viscous media. *Phys. Rev. E Stat. Nonlin. Soft Matter Phys.* **79**, 056307 (2009).
30. M. Palusa, J. de Graaf, A. Brown, A. Morozov, Sedimentation of a rigid helix in viscous media. *Phys. Rev. Fluids* **3**, 124301 (2018).
31. C. Kurzthaler, L. Zhu, A. A. Pahlavan, H. A. Stone, Particle motion nearby rough surfaces. *Phys. Rev. Fluids* **5**, 082101 (2020).
32. J. R. Blake, A. T. Chwang, Fundamental singularities of viscous flow. *J. Eng. Math.* **8**, 23–29 (1974).
33. W. E. Uspar, H. Burak Eral, P. S. Doyle, Engineering particle trajectories in microfluidic flows using particle shape. *Nat. Commun.* **4**, 2666 (2013).
34. R. N. Georgiev *et al.*, Universal motion of mirror-symmetric microparticles in confined Stokes flow. *Proc. Natl. Acad. Sci. U.S.A.* **117**, 21865–21872 (2020).
35. K. Kamrin, M. Z. Bazant, H. A. Stone, Effective slip boundary conditions for arbitrary periodic surfaces: The surface mobility tensor. *J. Fluid Mech.* **658**, 409–437 (2010).
36. H. Brenner, The slow motion of a sphere through a viscous fluid towards a plane surface. *Chem. Eng. Sci.* **16**, 242–251 (1961).
37. G. B. Jeffery, On the steady rotation of a solid of revolution in a viscous fluid. *Proc. Lond. Math. Soc.* **2**, 327–338 (1915).
38. W. R. Dean, M. E. O'Neill, A slow motion of viscous liquid caused by the rotation of a solid sphere. *Mathematika* **10**, 13–24 (1963).
39. H. Masoud, H. A. Stone, The reciprocal theorem in fluid dynamics and transport phenomena. *J. Fluid Mech.* **879**, 1 (2019).
40. L. G. Leal, *Advanced Transport Phenomena: Fluid Mechanics and Convective Transport Processes* (Cambridge University Press, Cambridge, UK, 2007), vol. 7.
41. M. E. O'Neill, K. Stewartson, On the slow motion of a sphere parallel to a nearby plane wall. *J. Fluid Mech.* **27**, 705–724 (1967).
42. R. G. Cox, H. Brenner, The slow motion of a sphere through a viscous fluid towards a plane surface—II Small gap widths, including inertial effects. *Chem. Eng. Sci.* **22**, 1753–1777 (1967).
43. Wolfram Research Inc., *Mathematica*, Version 12.3.1 (Wolfram Research Inc., Champaign, IL, 2021).
44. D. L. Chase, C. Kurzthaler, H. A. Stone, Data and codes for “Hydrodynamically induced helical particle drift due to patterned surfaces.” GitHub. https://github.com/ckurzthaler/materials_sedimentation_patterned_surface. Deposited 26 April 2022.